Sub-60°C atmospheric heliumwater plasma jets: modes, electron heating and downstream reaction chemistry

J J Liu, M G Kong

Sub-60^{o}C Atmospheric Helium-Water Plasma Jets: Modes, Electron Heating and Downstream Reaction Chemistry

J J Liu and M G Kong[1]

Dept of Electronic and Electrical Engineering, Loughborough University, Leicestershire LE11 3TU UK

Abstract

For plasma treatment of many heat labile materials (e.g. living tissues) that are either moist or contain a surface layer of liquid, it is desirable that the gas plasma is generated at atmospheric pressure for process convenience and with a gas temperature ideally no more than 60^{o}C for mitigating permanent damage to the integrity of the test material. This implies that the liquid-containing plasma needs to be of low energy and that plasma treatment should be based largely on non-equilibrium reaction chemistry. In this contribution, a class of sub-60^{o}C atmospheric helium-water plasma jets is studied in terms of their main physiochemical properties. It is shown that there are five distinct modes appearing in the sequence of, with increasing voltage, the first chaotic mode, the plasma bullet mode, the second chaotic mode, the abnormal glow mode, and the nonthermal arc mode. Its chaotic modes may be sustained over a wide range of water vapour concentration (0 – 2,500ppm). Compared to other liquid-containing plasmas, the He-H_2O plasma jet operated below its nonthermal arc mode has several distinct advantages, namely very low energy consumption (2 – 10 μJ per pulse), sub-60^{o}C gas temperature, electron-modulated production of He, N_2, N_2^+, O^*, H and OH(A-X), and low ozone production (0.1 – 0.4 ppm). These results provide a first attempt at the landscape of the physiochemical characteristics in atmospheric He-H_2O plasma jets.

[1] Corresponding author; e-mail: m.g.kong@lboro.ac.uk

1. Introduction:

Liquid-containing gas plasmas generated at or around atmospheric pressure have been studied for many decades, driven by many industrial and environmental applications such as electrical insulation, electrochemical analysis, waste water treatment, and nano-structure fabrication [1]-[5]. For most liquid-containing gas plasmas used in these applications, electrical energy sustaining their generation is usually very large, sometimes in excess of 25 kJ per electrical pulse [3]. As a result, they create an array of highly interacting and complex physiochemical processes including dynamic deformation of the gas-liquid-plasma interface, liquid vaporization, shock and acoustic wave, and considerable heat generation. These strongly coupled processes are at the root of some of the most intriguing phenomena, for example, dynamic phase transition [6] and single-bubble sonoluminescence [7].

Recent times have witnessed growing interest in biomedical applications of liquid-containing plasmas, due to a combination of biological effects of ionized gases and the aqueous environment of living tissues that is always present in plasma-tissue interactions [8]. Nonthermal atmospheric plasmas, so far interpreted broadly with a gas temperature as high as 7,000 K [3][9], have indeed found applications in medicine and these include blood and tissue coagulation [10][11], lithotripsy [12], and tissue removal [13], some of which have already become a routine clinical procedure. A common feature of these successful medical applications is that liquid-containing plasmas are used as a destructive step to break down an unwanted solid matter (e.g. kidney stone [14]) or colloidal matter (e.g. malignant tissue). This requires a physical force to be established by plasma in the form of localized heat release and/or shock wave. These plasma-based surgical procedures take up to a few tens of minutes to complete. More recent interest has been to mitigate damages to healthy tissues by reducing the reliance on plasma-established physical forces [15].

Provision of localized physical forces represents only part of a wide range of biological effects of nonthermal atmospheric plasmas [8]. Due to their antimicrobial and antitumor properties [8][16], they are increasingly studied and developed for low-temperature treatment of many diseases including skin and wound infection, chronic and acute wounds, and cancers and tumors [8][16][17]. Here reactive plasma chemistry provides the dominant biological effect with a timescale of as short as a few seconds, and the destructive physical force of the plasma is no longer beneficial. Low-energy liquid-containing atmospheric plasmas are therefore desired. Permanent damage and collagen denaturation are known to start to occur to skin at approximately 55^{o} – 65^{o}C [18][19]. Therefore the ceiling of the gas temperature should ideally be not much above 60^{o}C, as an indicator of the 55^{o} – 65^{o}C range, for safe plasma treatment of living tissues. This choice of the ceiling temperature is appropriate also for other heat-labile materials such as plant tissues, organic matters, and plastics [20].

Most liquid-containing atmospheric plasmas reported so far have a much higher gas temperature than 60^{o}C at the core of the plasma [3][9], and as such is not directly amendable for treatment of heat-labile materials. Although gas temperature may be reduced by increasing the plasma-sample distance or the flow rate of the plasma-forming gas, such methods can reduce considerably concentrations of reactive plasma species arrived at the surface of the heat-labile sample. For plasma treatment of living tissues, it is an important consideration since short-living reactive plasma species such as hydroxyl radicals and singlet oxygen are known to be important in plasma-mediated bactericidal effects [21]-[26]. This consideration is also true for plasma treatment of plastics and organic materials. Clearly, there is a general need for sub-60^{o}C atmospheric liquid-containing plasmas for treatment of many heat-labile materials. At present, this is a largely unexplored area partly because the benefits of liquid plasma reaction chemistry (e.g. those mediated by hydroxyl radicals and hydrogen peroxides) are only beginning to become clear [8]. Yet despite of few reported studies so far, sub-60^{o}C atmospheric liquid-containing plasmas should be feasible since near room-temperature atmospheric plasmas in other electronegative gases (e.g. air) have been realized successfully using, for example, nanosecond-pulsed excitations [27][28] or microplasma jets [29][30].

At present, it is little known what reaction chemistry may be most desirable for any given application and this uncertainty extends to the chemical composition of the plasma-forming gas (e.g. liquid-containing

helium, argon, nitrogen or air) [31]. For treatment of living human and plant tissues, the consideration of efficacy, safety and selectivity are more important than that of the cost of the plasma treatment. Given these, we consider in this contribution helium-water mixture as the plasma-forming gas with which to realize a sub-60^{o}C atmospheric plasma jet using a conventional AC power supply in the 10 – 100 kHz range. This study is intended to lead to similar studies of sub-60^{o}C atmospheric plasmas in other water-containing gases, for which the use of pulsed excitation may become necessary [32], so that similarities and contrasts of reaction chemistry provided by different plasma–forming gases could be unraveled to inform their use for different applications. For the convenience of discussion thereafter, this study is placed in a loose context of plasma treatment of living tissues. However its results should be directly applicable to other heat-labile materials.

To explore as broadly as possible the scope of reaction chemistry of atmospheric He-H_2O plasma jets, we consider varying both the applied voltage and the water content. The latter is controlled by splitting the helium flow into two channels with one fed through a water bubbling system and the other uninterrupted before being recombined as the plasma-forming gas with a fixed total flow rate of 4 slm (standard liter per minute). The primary goal here is to unravel main physical and chemical characteristics of the atmospheric He-H_2O plasma jet around the critical gas temperature of 60^{o}C so that the study lays down a solid scientific foundation with which to explore its low-temperature applications. From a plasma science standpoint, such He-H_2O plasma jets bridge the traditional pin-to-plate liquid-containing plasmas [3][33] and the cold atmospheric plasma (CAP) jets formed in a dry gas flow [34]. It is of interest whether their plasma characteristics resemble those of the two more studied atmospheric gas discharges and whether they may exhibit some unique properties of their own. As will be shown below, the atmospheric He-H_2O plasma jet has five modes of operation, each having distinct physical and chemical characteristics.

2. Experimental Setup:

The experimental setup is illustrated in Fig. 1 with an AC power supply having a peak-to-peak voltage ($V_{p\text{-}p}$) of up to 7kV at 20 kHz. The electrode unit consists of a powered capillary electrode, through which the helium-water gas is fed, and a grounded ring electrode and a downstream grounded stainless-steel plate electrode. The outer diameter of the capillary electrode is only slightly smaller than the inner diameter of the quartz tube, and the plate electrode is 10 mm downstream from the nozzle of the quartz tube. Since the main component of the electric field is in parallel to the gas flow, this is a linear-field plasma jet [35] and it can be up-scaled in an array of many parallel plasma jets for treatment of large and three-dimensionally structured objects (e.g. surgical forceps and human hands) [36][37]. Its electrode unit is detailed elsewhere [37]. The flow rate of the moist helium channel, F_{moist}, varies from 0 (i.e. dry helium) to 400 sccm (standard cubic centimeter per minute). The maximum F_{moist} corresponds to a water concentration of 2,500 ppm, estimated using data in literature [38]. The plasma image in Figure 1 shows a visually streamer-free discharge formed between the powered capillary electrode and the ground downstream plate electrode. This plasma stability is in sharp contrast to that in high-energy liquid-containing plasmas [3], but similar to jet plasmas formed in a dry He-containing gas flow [37].

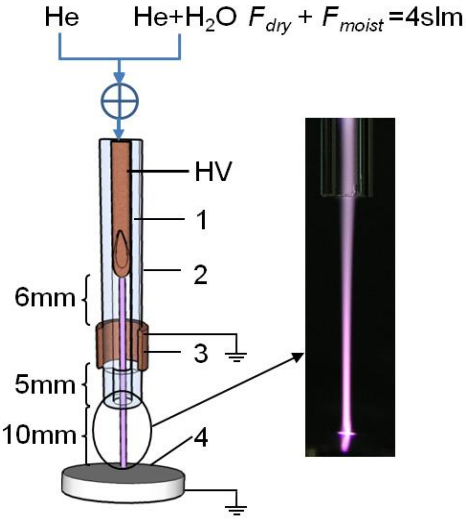

Figure 1: Schematic of the capillary-ring electrode configuration and an image of a plasma jet in an atmospheric He/H_2O flow. The capillary, the ring, and the downstream plate electrodes are labelled as 1, 3 and 4, respectively, whereas the quartz tube is marked as 2.

For treatment of living tissues, the upstream introduction of large quantity of water vapor is motivated by the need to achieve reproducible plasma-mediated non-equilibrium chemistry on the site of a malignant tissue. One source of variations comes from the liquid layer on the surface of an infected skin or an open wound,

which varies significantly from one case to another. This introduces variation to the plasma interaction with the liquid layer covering the living tissue and indeed the resulting biological effects. It may be mitigated by, for example, firstly wiping and/or gas drying before plasma treatment. Then the remaining water content on the tissue surface can be made negligible by introducing larger quantity of water vapor into the upstream plasma generation region some distance above the tissue surface. As a result, plasma chemistry involving water molecules takes place predominately in the upstream electrode region (see Fig. 1), affected little by the inevitably variable liquid content on the tissue surface.

It is worth comparing the atmospheric He-H_2O plasma jet in Fig. 1 with several similar liquid-containing jet plasma sources. Atmospheric plasma jets in a dry gas flow and with a downstream aqueous ground electrode is clearly different, since the H_2O-participating chemistry takes place in the downstream liquid layer and vaporization of the liquid layer is common [39]-[42]. Sharing some similarities with that in Fig. 1, atmospheric plasmas having a carrier gas pre-mixed with liquid aerosol are often used as a detector for gas chromatography [43], for analysis of liquid sample by means of atomic absorption and emission [44], and for surface modification in the plasma generation region [45]. With the liquid aerosol containing precursor chemicals, these plasmas have very different plasma chemistry from the atmospheric He-H_2O plasma jet. It is worth noting that similar setup to that in Fig. 1 has been used in studies of atmospheric Ar-H_2O plasma jets excited at 13.56 MHz [46] and at 71 kHz [47] with rotational temperature being 1,100K and 620 – 1,125K, respectively. These argon plasmas have much greater gas temperature than 60^{o}C and as such are more appropriate to applications for which high gas temperature is not hindering. Argon is known to lead to high gas temperature [48][49], though this could be mitigated with sub-microsecond pulsed excitation [48].

3. Electrical Characterization and Plasma Modes:

Using common electrical techniques for cold atmospheric plasmas [37], the applied voltage is measured together with the discharge currents flowing through the ring electrode (marked in blue in Fig. 2) and through the downstream plate electrode (in red). Fig. 2 shows the case of F_{moist} = 20 sccm over a wide voltage range from shortly after plasma ignition to the point where the plasma becomes unstable with a significant temperature rise. The peak discharge current is in the range of 2 – 10 mA, clearly less than those of the Ar-H_2O plasma jets (>50mA) [46][47] and much lower than those of traditional nonthermal liquid-containing plasmas (1 – 1000 A) [3][9]. This comparison remains true for the current density also, and so the He-H_2O plasma jet of Fig. 1 is likely to possess different properties to traditional nonthermal liquid-containing plasmas. It is evident that the current waveform undergoes a sequence of distinct changes as the applied voltage increases, indicating the presence of different operation regimes or modes and their transition. These are examined here using electrical properties of the plasma and its nanosecond images.

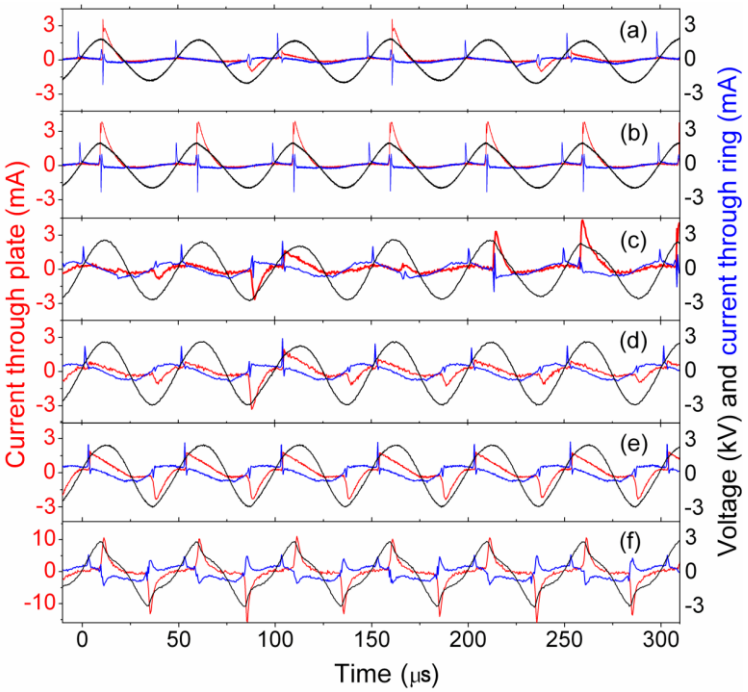

Figure 2: Waveforms of the applied voltage (black), the current flowing to the plate electrode (red), and the current flowing to the ring electrode (blue) in (a) the first chaotic mode; (b) the bullet mode; (c) the second chaotic mode near the bullet mode; (d) the second chaotic mode near the arc mode; (e) the abnormal glow mode with no voltage distortion; and (f) the nonthermal arc mode with voltage distortion.

Figure 2a shows a weak discharge shortly after breakdown and with non-periodic current waveform. The cycle-to-cycle evolution of its discharge current shows clear features of chaos (data now shown), and is very similar to that in the chaotic mode of an atmospheric dry-helium plasma jet also at low discharge currents [50]. This is the first chaotic mode of the He-H_2O plasma jet. In Fig. 2b, the discharge current becomes periodic and its waveform is typical of that when a discrete train of bullet-like and moving emission spots, the so-called plasma bullet, is formed on a nanosecond scale [34]. As will be confirmed with nanosecond imaging (see Fig. 4 and its discussion below), this is the bullet mode. With increasing applied voltage, the discharge current again becomes non-periodic in Fig. 2c and 2d and their cycle-to-cycle behaviors are similar to that of the chaos mode observed in dry-helium flow [50] and that in Fig. 2a. This is the second chaotic mode at higher dissipated power than that in Fig. 2a (see discussion of Fig. 3 below). For both chaotic modes, their power spectra are continuous function of frequency and peaks in the spectra do not disappear with increasing data points. Their phase portraits over a few hundreds of excitation cycles do not resemble limited cycles but a complex structure and their Poincare sections appear as a horseshoe structure (data not shown), both indicative of deterministic chaos and both similar to the characters of the chaos mode in a dry He atmospheric plasma jet [50]. Detailed analysis of chaos requires full consideration of phase portrait and Lyapunkov exponent. This is outside the scope of the present study and will be addressed in a future note. It is worth noting that the presence of two chaotic modes on either side of the bullet mode was not discussed in the first report of chaos in atmospheric plasma jets in a dry gas flow [50]. This has since been observed in atmospheric dry helium plasma jets [51]. So they are generic to atmospheric helium-containing plasmas.

Further increase in the applied voltage leads to the current waveforms returning to periodic in Fig. 2e – 2f, where the current is no longer pulse-like but persists continuously throughout one entire period of the applied voltage. Similar to those observed in atmospheric helium plasma jets [50], these are known as the continuous mode in atmospheric plasmas in dry gases [50] with that in Fig. 2f having unstable plasma filaments and non-sinusoidal voltage waveform. As will be shown below, the discharge current increases with increasing voltage in Fig. 2e whereas it increases with decreasing voltage in Fig. 2f. These are similar to properties of the abnormal glow and the nonthermal arc modes in low-pressure dc plasmas. Therefore they are referred to as the abnormal glow mode (Fig. 2e) and the nonthermal arc mode (Fig, 2f), respectively.

Electrical characteristics of the five plasma modes of Fig. 2 and their mode transition are more clearly seen in the voltage dependence of the dissipated plasma power, obtained from averaging the product of the applied voltage and the total current. The use of the dissipated power in the place of the discharge current is due to considerable distortion to the current waveform. However if a suitable value is used to represent the discharge current, the current-voltage dependence is likely to be very similar to the power-voltage dependence. As illustrated in Fig. 3, all five modes are present in an appearance sequence of, with increasing voltage, the first chaotic mode, the bullet mode, the second chaotic mode, the abnormal glow mode and the nonthermal arc mode when F_{moist} < 100 sccm. Under such low H_2O-content conditions particularly when F_{moist} < 40 sccm, the power-voltage relationship is very similar to that with dry helium flow (i.e. F_{moist} = 0 sccm). In the two chaotic modes, the bullet mode, and the abnormal glow mode, the dissipated power increases with the applied voltage. By contrast, the dissipated

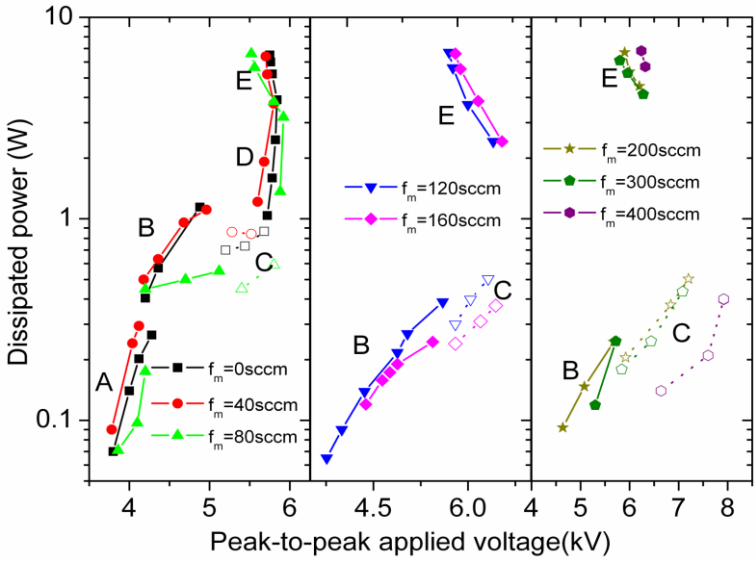

Figure 3: Dissipated power as a function of the applied voltage at different F_{moist}. Mode *A*, *B*, *C*, *D*, and *E* are used to refer to the first chaotic mode, the bullet mode, the second chaotic mode, the abnormal glow mode and the nonthermal arc modes, respectively.

power increases with decreasing voltage in the nonthermal arc mode. It should be noted that the use of water vapour inevitably deposits a water layer on the surface of the ground electrode and that the ring electrode is dielectrically insulated from the power electrode by the quartz tube. This suggests that the plasma formed with the setup in Fig. 1 is in fact dielectric barrier discharges (DBD). With parallel-plate electrodes and atmospheric helium, the Townsend and the normal glow modes are the common DBD modes that can be observed with cycle-to-cycle reproducibility [52][53]. The use of the flowing gas in the DBD configuration appears to have broadened the available discharge modes.

Further increase in water concentration towards F_{moist} = 120 sccm sees the disappearance of the first chaotic mode and the abnormal glow mode. Now there are only three modes (i.e. the bullet, the second chaotic and the nonthermal arc mode). As the moist helium flow rate increases, the second chaotic mode is seen to persist over a wider range of the applied voltage and its dissipated power reduces to become comparable to that of the bullet mode. The presence of a chaotic mode in liquid-containing atmospheric plasmas has not been reported, nor has its persistence over a large water content range (0 – 2,500 ppm). In many ways, this is counter-intuitive since chaos is in general difficult to observe experimentally in a strongly driven system (e.g. periodic electrical excitation) that is open to persistent perturbations (e.g. ambient condition fluctuations). The introduction of large quantity of water vapour could readily smear or disrupt the evolution of necessary nonlinear processes required for the development of chaos. Yet Fig. 3 suggests a persistent chaotic mode over a larger F_{moist} range, and this needs to be further studied to identify possible mechanisms. Also indicated in Fig. 3 is a co-existence between the chaotic and the arc modes at a given applied voltage. As the arc mode consumes much higher electrical power, a power-limiting technique may be used effectively to control transition to the arc mode. In other words, mode selection and locking is achievable.

Plasma jet formation is often considered to be linked to photon ionization, and its explanation is often based on the seminal work of Dawson and Winn in 1965 [54]. In the Dawson-Winn model of photon ionization [54]-[56], a plasma bullet is viewed as the positively charged head with n_+ positive ions of a cathode-directed streamer. Photon emission from the streamer produces new electrons and positive ions in front of itself. To form a plasma bullet, it is necessary that the number of the newly produced positive ions by photon ionization must be equal to n_+ [54]. At a fixed applied voltage, water molecules are likely to reduce the level of gas ionization. Being electronegative, water molecules introduce an added electron loss mechanism. Both effects are expected to reduce the amount of the positive ions in the head of a plasma bullet at a given applied voltage. While photon ionization is also expected to become less effective and produces less new electron-ion pairs, it is not immediately clear that the new ions produced would remain balanced out by n_+. Yet plasma bullets are formed at the same applied voltage, for example at $V_{p\text{-}p}$= 5kV as shown in Fig. 4, over a wide range of water concentration from 0 to 1,950 ppm (F_{moist} = 0 – 300 sccm). These results appear to suggest that the Dawson-Winn model [54] would need further examination and other possible mechanisms

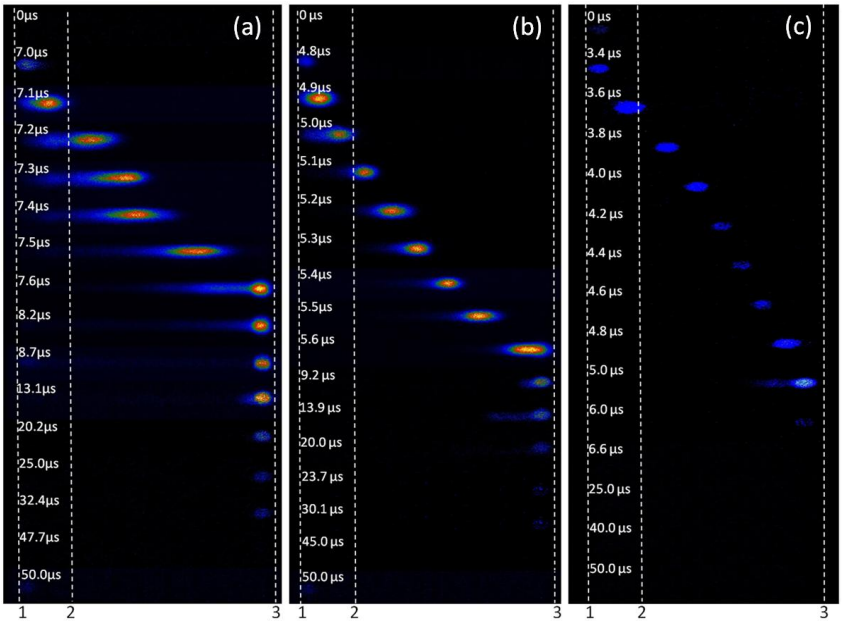

Figure 4: Nanosecond images (10ns) of the He/H_2O plasma jet in its bullet mode when F_{moist} is (a) 0 ppm (at 0.7 W and $V_{p\text{-}p}$ = 5kV); (b) 400 ppm (at 0.4 W and $V_{p\text{-}p}$ = 5kV); and (c) 1950 ppm (at 0.24 W and $V_{p\text{-}p}$ = 5.8kV). Label 1, 2, and 3 mark, respectively, the locations of the ring electrode, the tube nozzle, and the ground plate electrode.

should not be ruled out. With increasing H_2O concentration and at a fixed voltage, the dissipated power in the bullet mode is seen to decrease in Fig. 3 and this is consistent with the decreasing optical emission of the plasma bullet in Fig. 4a and 4b.

The nonthermal arc mode exists for all water concentrations studied and its dynamics are considered here. Fig. 5 shows its plasma appearance on a nanosecond scale of 10 ns over one complete cycle of the applied voltage. The plasma is no longer bullet-like, and its light emission appears over the entire length of the inter-electrode gap. Its discharge current through the downstream plate electrode persists over the whole period of the applied voltage (Fig. 2f). In the positive half cycle, the development of the plasma jet seems to suggest a cathode-directed propagation with the images at 2.8, 3.2 and 3.6 μs showing a clear evolution of plasma dynamics. In the negative half-cycle, on the other hand, images show less clear evolution pattern of plasma dynamics.

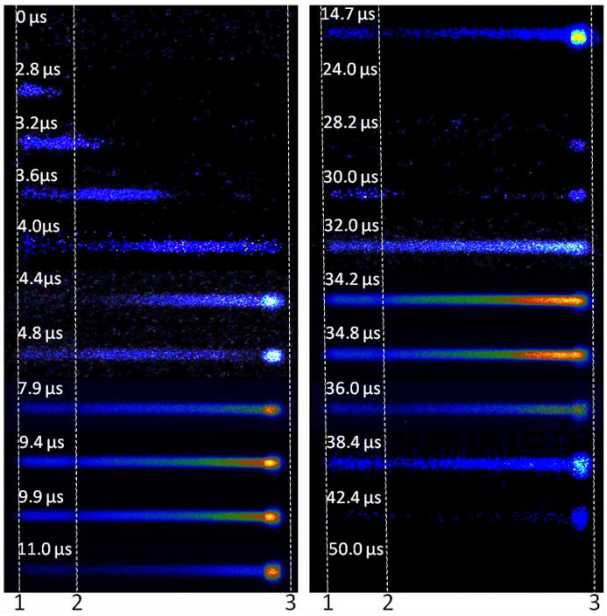

Figure 5: Nanosecond images of the atmospheric He/H_2O plasma jet in its nonthermal arc mode at $V_{p\text{-}p}$=5.8kV, P = 4.5 W and F_{moist} = 0 sccm. The left panel is for a positive half cycle, and the right is for the next negative half cycle. Exposure time is 10 ns.

Modes of the atmospheric He-H_2O plasma jet and their transition are discussed above in terms of its dissipated power and its implication for gas ionization, electron production and electron heating (see discussion below on electron density and electron temperature). For other atmospheric liquid-containing plasmas, modes in terms of whether the plasma is formed within water bubbles are recently reported [57].

It is of interest to discuss the dissipated electrical energy in the plasma. In the bullet mode, the current flowing through the plate electrode has a sharp pulse of 10 – 12 μs (Fig. 2b) and the dissipated power of 0.2 – 0.8 W (Fig. 3) is mostly consumed during the current pulse. The electrical energy is therefore 2 – 10 μJ per pulse. In the nonthermal arc mode, the current waveform is continuous and so the half period is used as an effective pulse width. At 20kHz, the half period is 25 μs with which the consumed electrical energy is estimated to be 200 μJ per pulse at a dissipated power of 8W (Fig. 3). Therefore the energy consumption of the atmospheric He-H_2O plasma jet is at most 2 – 200 μJ per pulse, some 4 – 6 orders of magnitude below that of the liquid-containing corona discharges and 7 – 10 orders below of the liquid-containing pulsed arcs [3]. In its bullet mode, the energy consumption of the He-H_2O plasma is slightly less than 5 – 35 μJ per pulse estimated for the 71 kHz Ar-H_2O plasma jet [47] and comparable to 5 μJ per half cycle estimated for the 13.56 MHz Ar-H_2O plasma jet [46]. These plasma jets represent a relatively new class of low-energy atmospheric liquid-containing plasmas appropriate for low-temperature applications.

4. Plasma Temperatures and Electron Density:

Non-equilibrium plasmas are usually characterized by at least five temperatures, namely the electron temperature (T_e), the rotational temperature (T_{rot}), the vibrational temperature (T_{vib}), the translational temperature (T_{tran}), and the electronic excitation temperature (T_{exc}). These are useful to describe electron kinetic properties and their implications to plasma chemical reactions and to the global plasma properties (e.g. gas temperature). At atmospheric pressure, the rotational temperature may be used to approximate the gas temperature since the collision frequency of molecules with heavy particle is very high (~ THz) and rotational relaxation is fast [58]. For non-equilibrium plasmas sustained by an externally applied electric

field, reliable diagnostics of electron temperature such as Thomson's scattering are not easily accessible and as a result the vibrational or excitation temperatures of certain molecular species (OH or N_2) is sometimes used as an indirect indicator of T_e. For low-temperature atmospheric plasmas, $T_e > T_{vib} > T_{rot} = T_{tran}$ [59] is usually true and $T_e = T_{exc}$ may not be universally assumed [58]. For T_{rot} and T_{vib}, they may be measured together from comparing a measured molecular spectrum of the plasma with its synthetic spectrum.

Here we use the N_2 second positive system ($N_2C^3\Pi_u \rightarrow X^2\Pi_g$, 360–388nm) to estimate T_{rot} and T_{vib} with the synthetic spectrum obtained using SPECAIR [58]. For T_e of non-equilibrium atmospheric plasmas, the most accurate technique is perhaps laser Thomson scattering [60][61]. Since this and other similarly sophisticated diagnostics are not widely accessible, it is desirable to employ easily applicable techniques and obtain some indication T_e of by means of, for example, T_{exc}. For non-equilibrium plasmas, T_{exc} can be used only as an indicator of the ability of electrons to excite atoms to their excited states. This work is based on the work of van der Mullen and co-workers [62]-[64], to which the reader is referred. Here, a brief discussion is provided to describe the basic principle and its application. Consider the Boltzmann balance that describes the exchange of the internal energy of an atom with free electrons in an inelastic atom-electron collision. This leads to either an excitation of the atom or its de-excitation between two energy levels, j and k. If these two energy levels equilibrate and the free electrons may be assumed to have a Maxwellian energy distribution, the atomic state distribution function (ASDF) obeys the Boltzmann relation [62]-[64]

$$\frac{\eta_j^B}{\eta_k^B} = \exp\left(\frac{E_k - E_j}{kT_e}\right) \tag{1}$$

where $\eta_{j,k}{}^B$ is the Boltzmann population density of atom A in its energy level j or k, and E_k and E_j are the excitation energy of the atom at level j and k, respectively, k is the Boltzmann constant, and T_e is the electron temperature. Consider now the Saha balance that describes production and destruction of free electrons through ionization of an atom and electron-ion recombination. Involving an ionic state of the atom, A^+, and assuming that the ionization and recombination balance, the ASDF is described by the Saha formula [64]

$$\eta_j^S = \frac{1}{2}\eta_+ n_e \left[\frac{h^2}{2\pi m_e k T_e}\right]^{3/2} \exp\left(\frac{E_+ - E_j}{kT_e}\right) \tag{2}$$

Here $\eta_j{}^S$ is the Saha population density of atom A at level j, η_+ is the population density of ion A^+ in the ground state, E_+ is the ionization energy of the atom, n_e is the electron density, m_e is the mass of electron, and h is the Planck constant. By assuming $\eta_e = \eta_+$ (hence $n_e = n_+$) and by taking the natural logarithm of the above equation, we arrive at

$$\ln \eta_j^S = \frac{E_+ - E_j}{kT_e} + \ln \eta_\infty \tag{3}$$

where

$$\eta_\infty = \frac{1}{2} n_e^2 \left[\frac{h^2}{2\pi m_e k T_e}\right]^{3/2} . \tag{4}$$

Therefore if $\ln(\eta_j{}^S)$ is plotted as a function of $(E_+ - E_j)$, the value of T_e may be obtained from the slope of the plot and that of η_∞ may be obtained by a linear extrapolation of $\eta_j{}^S$. With the value of T_e, the value of η_∞ may be used to deduce n_e. As indicated above, T_e obtained this way is more close to T_{exc} rather than the actual electron temperature. When the ASDF applicable to all the energy levels obeys the Saha formula, the plasma is said to be in Local Saha Equilibrium (LSE) [65]. If only a part of the atomic system (i.e. some energy levels) is populated according to the Saha formula, this part of the atomic system is said to be in partial LSE (pLSE) [65]. These atomic levels are interrelated to each other by the Boltzmann relation. The excitation temperature determined from the relative or absolute population of these levels equals the electron temperature. In other words, T_e determined from the above method may be considered to be close to T_{exc}.

In a plasma experiment, the atomic population density on one particular energy level can be measured or inferred from optical emission spectroscopy. This is usually done in a plasma volume-averaged and time-averaged fashion, with which the electron density and electron temperature may be assumed as constants for all energy levels (i.e. mean electron energy and mean electron temperature). Similarly the ionic population

density may be assumed as constant as well. Therefore, η_∞ may be considered as constant, and may be plotted as a function of energy levels. This $\ln\eta_j \sim E_j$ relation should appear as a straight line with a negative slope of $-1/kT_{exc}$, from which T_{exc} may be deduced by linear extrapolation. The above discussion is based on the assumption of local thermodynamic equilibrium (LTE) [62], which is not satisfied in low-temperature atmospheric plasmas. An alternative indicator of the electron temperature may be obtained under partial LTE (pLTE) and pLSE conditions, by considering an excitation temperature, T_{13}, for the transition to the first easily measurable excited state [63]. In our experiments, this is associated with the helium emission at 706 nm to from level 2 to level 3. Clearly T_{13} should be less than T_e. Here the ASDF is constructed with the absolute density of the ground state and four excited helium state (i.e. 447.2, 587.6, 667.8, 706.5nm), and the elementary occupation of level k is given by [66]

$$\eta_k = \frac{4\pi I_{kj}}{A_{kj}E_{jk}Dg_k} \tag{5}$$

where I_{kj} is the transition integrated absolute intensity of relevant optical emission, A_{kj} is the spontaneous transition probability, and $E_{jk} = E_k - E_j$ is the difference between the lower and higher atomic energy levels. D is the plasma depth in the line of sight (i.e. the diameter of the plasma plume), and g_k is the statistical weight of level k. Values of g_k, E_{jk} and A_{kj} are estimated from the NIST data for the four excited helium states. The population density of the ground state, η_1, can be calculated by,

$$\eta_1 = n_1 / g_1 = p / kT_g g_1$$

and the population density at level 3, η_3, satisfies eq.(1), or

$$\eta_3 = \eta_1 \exp\left((E_1 - E_3)/kT_{13}\right) \tag{6}$$

Here the population density η_3 is obtained from eq.(5) with $I_{kj} = I_{32}$ corresponding to the transition integrated absolute intensity of optical emission at 706nm. Therefore by plotting $\ln(\eta_3)$ as a function of the excitation energy E_{13}, the resulting curve should be a straight line and its slope should be $(-1/kT_{13})$. This is known as the ASDF plot of an ionizing plasma. Figure 6 shows the ASDF in the bullet mode. The plasma volume whose light emission was picked up by the optical fibre of the spectrometer had a diameter of 0.64mm, across which the plasma emission intensity was largely uniform. The solid angle of the optical pickup was approximately 3×10^{-4} rad. On the other hand, self-absorption effects of the helium emission lines were not considered, and therefore the result shown in figure 6 is an approximate.

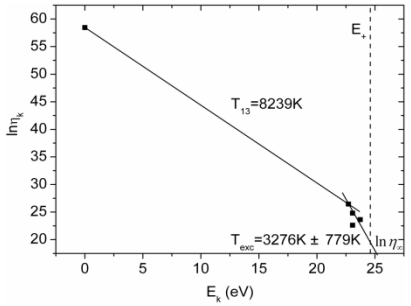

Figure 6: Plot of the atomic state distribution function for the atmospheric He-H_2O plasma jet in its bullet mode (V_{pp} = 5kV; F_{moist} = 0sccm). E_+ is the helium ionization energy.

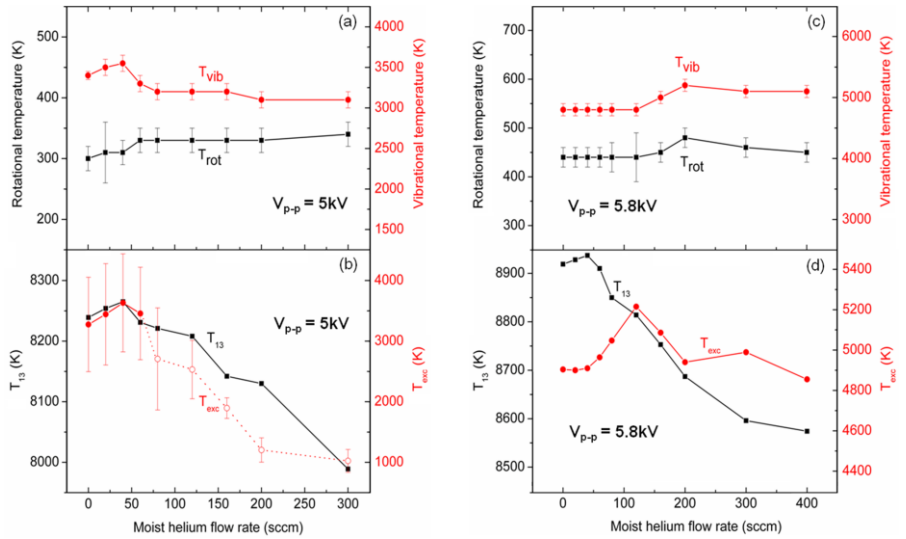

Figure 7: F_{moist} dependence of rotational temperature, vibrational temperature, excitation temperature, and T_{13} (the excitation temperature between the ground and the first excited state) at $V_{p\text{-}p}$ = 5kV within the bullet mode (in (a) and (b)) and at $V_{p\text{-}p}$ = 5.8kV within the nonthermal arc mode (in (c) and (d)).

Fig.7 shows the moist helium flow rate dependence of T_{rot}, T_{vib}, T_{exc} and T_{13} for one case each in the bullet mode and in the nonthermal arc mode. In the case of the bullet mode at V_{pp} = 5.0kV (Fig.7a and 7b), rotational temperature, T_{rot}, increases slightly from 300 K at F_{moist} = 0 sccm to 325 K at F_{moist} = 60 sccm after which it undergoes a small increase to ~ 335K at 300 sccm. This corresponds to 27 – 62°C for all moist helium flow rates studied, similar to those of atmospheric dry-He plasmas [32][67]. This temperature range is in general appropriate for sub-60°C applications to heat-labile materials. Similar to the $T_{rot} - F_{moist}$ dependence, the vibrational temperature also undergoes a small increase from

3,400 to 3,550 K in 0 – 40 sccm. Then it decreases to 3,200 K at F_{moist} = 80 sccm before levelling off at approximately 3,100K. For T_{exc} and T_{13}, the initial trend is also a small increase till F_{moist} = 40 sccm when they reach their maximum values of 3,632K and 8,265K, respectively. After that, they both decreases monotonically to reach 1,000K and 7,988 K at 300 sccm, respectively. For F_{moist} > 60 sccm however, helium emission lines at 447.2 nm and 587.6 nm are weak in the bullet mode thus affecting the reliability of the T_{exc} measurement. This is marked with dashed line in Fig. 7b. Its value of 3,200 – 3,632 K for 0 – 60 sccm is similar to those of atmospheric dry helium plasmas [68]. Despite of the uncertainty of T_{exc} for F_{moist} > 60 sccm, its trend of an initial rise and then decay is unambiguous in Fig. 7b. This suggests an effective electron heating with increasing water concentration till 40 sccm (or 250 ppm), perhaps benefited from a similar trend of the dissipated power (see Fig. 8a), in the bullet mode.

In the 0 – 60 sccm range, T_{exc} = 3,200 – 3,632 K and T_{vib} = 3,400 – 3,550 K and they are therefore comparable. For atmospheric dry helium plasmas, the mean electron temperature is reported to be about 1 – 5 eV [69][70]. Therefore T_{13} of 7,988 – 8,265 K in Fig. 7b is closer to T_e in value than T_{exc}. It is worth re-emphasizing that T_{13} is obtained under pLSE conditions and for the first measurable excited state of the helium atom. It should therefore be smaller than T_e. It is interesting to note that T_{vib}, T_{exc} and T_{13} all increase first to reach their maximum values at 40 sccm and then start to decrease. At a constant applied voltage (V_{p-p} = 5.0 kV), this appears to suggest that electrons efficiently exchange energy with helium atoms with increasing moist flow rate from 0 to 40 sccm. The subsequent fall in T_{vib}, T_{exc} and T_{13} may indicate a reduced energy exchange, possibly related to an increase in electron attachment to water molecules and to a reduced level of gas ionization at a constant applied voltage.

In the nonthermal arc mode at V_{p-p} = 5.8kV (Fig. 7c and 7d), the rotational temperature initially remains at 445K for 0 – 120 sccm, then from 120 sccm increases to reach its maximum value of 480K at 200 sccm, and finally from 200 sccm undergoes a gradual reduction to 450K at 400 sccm. The trend of an initial increase followed by a gradual decay in 120 – 400 sccm is similar to that in the bullet mode, but the transition point in the arc mode occurs at a much higher moist flow rate of 200 sccm. The rotational temperature of less than 480K confirms the nonthermal character of the arc mode in Fig. 2f. Its value is nevertheless 145K above the rotational temperature in the bullet mode and is well above 60^{o}C thus inappropriate for treatment of living tissues. Yet it is still considerably below those observed in Ar-H_2O plasma jets of 620 – 1,125 K [46][47]. Even with comparable energy consumption of 2 – 35 μJ per pulse, this low gas temperature in the helium plasma is not surprising because of the better thermal conductivity of helium.

Of interest is that the vibrational temperature in the nonthermal arc mode follows an identical trend to its corresponding rotational temperature with the transition point also at 200 sccm. The value of the vibrational temperature in the arc mode is between 4,800 and 5,200 K, some 400K above that in the bullet mode. The similarity in the F_{moist} dependence of T_{rot} and T_{vib} in the bullet mode is less but nevertheless remains close.

Similar to the F_{moist} dependence of T_{13} in the bullet mode (Fig. 7b), T_{13} in the arc mode reaches its maximum value also at 40 sccm. Its value range varies in the range of 8,570 – 8,940 K, and is about 520 – 580K above its corresponding value in the bullet mode. In the arc mode, the electronic excitation temperature, T_{exc}, evolves initially as a constant of 4,900 K in the range of F_{moist} = 0 – 40 sccm before climbs to its maximum value of 5,200K at 120 sccm, where its corresponding T_{rot} and T_{vib} start to increase. Subsequently in the 120 – 200 sccm range, T_{exc}, undergoes a monotonic decrease to 4,920 K at 200 sccm after which it changes little between 4,850 and 5,000 K. Its final plateau in the 200 – 400 sccm range may not be compared to that in the bullet mode due to the weak helium emission intensities of the latter. The maximum value of T_{exc} in the arc mode is about 1,550K above its value in the bullet mode.

To explain the moist flow rate dependence of T_{vib}, T_{exc} and T_{13} in Fig. 7, the dissipated power, P, is obtained from averaging the product of the applied voltage and the total current over time and is shown in Fig. 8a. Electron density n_e is also estimated from calculating the total charge flowing to the plate electrode from the

discharge current and dividing it by the volume of the plasma plume. The results are shown in Fig. 8b with n_e = 4.9 – 15.4 x10^{12}cm^{-3} in the bullet mode and 1.8 – 3x10^{13}cm^{-3} in the nonthermal arc mode. Alternatively, electron density may be obtained from η_∞ in eq.(2), for which the electron temperature at the surface of the plate electrode may be assumed to be ~ 1eV. This method results in a maximum n_e of 0.4 – 6 x10^{13}cm^{-3}, similar to the n_e = 0.5 – 3 x10^{13}cm^{-3} range for both the bullet and the arc modes in Fig. 8. These estimates are also consistent with $n_e \leq$ 2x10^{13} cm^{-3} for a discharge current <10mA, measured using laser heterodyne interferometry [71].

In the bullet mode, n_e = 4.9 – 15.4 x10^{12}cm^{-3} and P = 0.01 – 0.9 W. Both the dissipated power and the electron density are seen to follow a very similar trend, namely an initial increase to reach their perspective peak value at 40 sccm (or ~ 250 ppm) followed by an exponential-like fall. Resembling closely the F_{moist} dependence of T_{vib}, T_{13} and T_{exc} with the same transition point at 40 sccm (see Fig. 6a – 6b), Fig. 8a and 8b suggest that electron heating and electron production increase with increasing dissipated power till 40 sccm. An increase in the dissipated power is likely to increase gas ionisation via Penning ionization processes by helium metastables, particularly $He^*+H_2O \rightarrow He+H_2O^+ + e$, $He^*+H_2O \rightarrow He+ OH^+ + H + e$, $He^*+H_2O_2 \rightarrow He+OH+OH^+ + e$ [72]. A recent global modeling of atmospheric He-H_2O plasmas suggests that electron generation is predominately due to Penning ionization of H_2O, electron impact ionization of helium, and metastable pooling of helium species and that the electron generation rate peaks between 30 – 100 ppm [72]. In the bullet mode, the simultaneous reach to the maximum value of n_e, T_{exc} and T_{13}, and P at 40 sccm or 250 ppm is therefore consistent with the prediction of the global model.

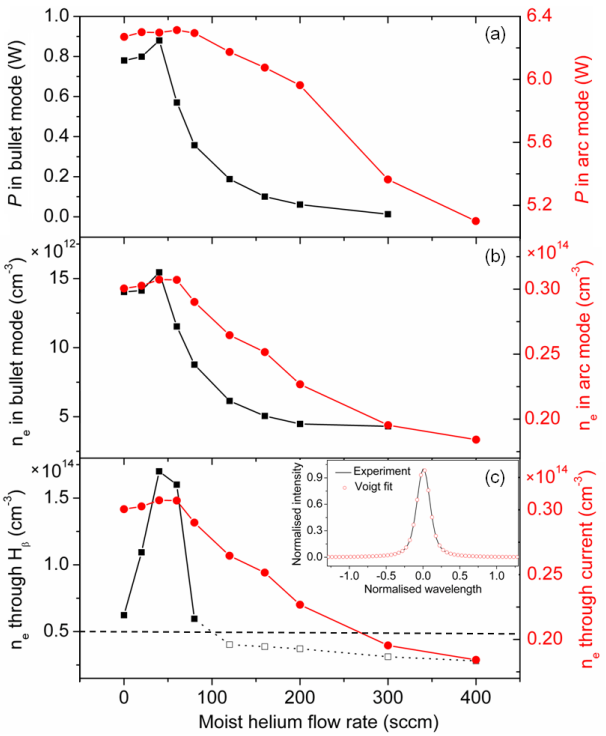

Figure 8: F_{moist} dependence of (a) dissipated power; (b) electron density measured from discharge current; and (c) electron density measured from Sark broadening in the nonthermal arc mode. In the bullet mode (black), V_{p-p} = 5 kV; and V_{p-p}=5.8kV in the high-current arc mode (red).

In the nonthermal arc mode, the initial increase in n_e (1.8 – 3.0 x10^{13}cm^{-3}) and P (5.1 – 6.3 W) is very modest and their subsequent fall from 60 sccm is also more gradual in comparison to the bullet mode. As n_e = 3 x10^{13}cm^{-3} is close to ~5×10^{13} cm^{-3} above which Stark broadening may be used to measure electron density, we consider the latter method for the arc mode. Specifically n_e may be evaluated from the line-shape of the Balmer β transition (4-2) of atomic hydrogen with the related emission at 486nm (H_β line) [73]. Although the H_α line (at 656nm) has higher intensity than H_β, it is rarely used to measure low electron density due to its sensitivity for self-absorption and strong broadening by ion dynamics [74]. We first estimate various broadenings including Van der Waals, Doppler, resonance, natural and instrumental broadenings, and their combination broadening is 0.035 – 0.045 nm, which can be resolved using our spectrometer. Results using Stark broadening are shown in Fig. 8c and indicate a peak electron density of 1.7x10^{14}cm^{-3} in the 40 – 60 sccm range (or 250 – 400 ppm). The moist helium rate at which n_e reaches its peak value is the same regardless of its measurement techniques, but that estimated using the H_β line is higher.

It is worth noting that electron density estimated for a comparable atmospheric Ar-H_2O plasma jet is about 1.5x10^{13} cm^{-3}[47], similar to the upper end of the electron density range of the atmospheric He-H_2O plasma jet in its bullet mode. Given that the maximum energy consumption is 10 μJ per pulse in the He-H_2O plasma

jet and 35 μJ per pulse in the Ar-H_2O plasma jet, it appears that the former is more efficient in electron production at a lower gas temperature (i.e. less energy conversion into heat).

5. Reactive plasma species:

The key benefit of sub-60°C atmospheric liquid-containing plasmas is to deliver controlled reaction chemistry to a downstream location. To this end, it is important to characterize main reactive plasma species arrived at the surface of the ground electrode (see Fig. 1) where the sample is usually placed. So far there has been little characterization of downstream reaction chemistry for low-energy atmospheric liquid-containing plasmas, and the only information in literature appears to be a monotonic decrease of optical emission intensities, with increasing water content, of excited atomic oxygen at 777nm, excited OH (A-X) at 309 nm, and exited argon atom at 696, 763 and 801 nm, respectively, in an atmospheric Ar-H_2O plasma jet [47]. This is therefore a considerably under-studied area. To provide comparison with future studies, absolution emission measurement is made in the 350 – 850 nm range and simultaneous relative emission measurement in the 200 – 900 nm. As absolution emission measurement below 350nm is unavailable at the point of this investigation, the relative intensity data provide an indirectly calibrated extrapolation of absolute emission intensities spanning across the visible range.

Fig. 9 shows the H_2O dependence of optical emission intensities of atomic oxygen lines at 777 and 845 nm, helium line at 706 nm, N_2 line at 358, 317, 337 nm, N_2^+ line at 391 nm, and H line at 656 nm, in the bullet mode at V_{pp}= 5kV. The strongest emission is from N_2 line at 358nm, and it reaches 0.6μW/cm^2. In Fig. 9a, all emission intensities increase first then decrease and all have their maximum intensity at F_{moist} = 40 sccm. This is identical to the point where both the electron density (see Fig. 8b) and the electron excitation temperatures (see Fig. 7b) reach their respective maxima. The same trend is seen in Fig. 9b for two other N_2 lines, the H line at 656 nm, and the OH line at 309 nm, indicating a strong correlation to electrons. This suggests that production of these species is directly correlated to electron density and/or electron temperature, or directly related to electron heating.

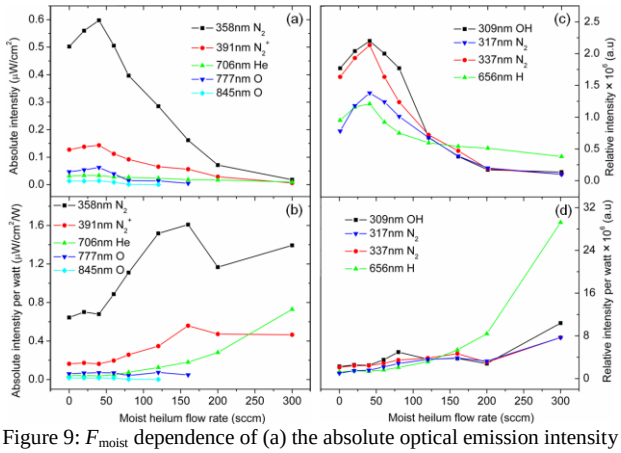

Figure 9: F_{moist} dependence of (a) the absolute optical emission intensity above 350 nm; (b) the absolute intensities per watt of dissipated power; (c) the relative optical emission intensities; and (d) the relative optical intensity per watt, all in the bullet mode at V_{p-p} = 5 kV.

For F_{moist} > 40 sccm, the emission intensities are seen to decrease for all excited species considered. This may be related to the decrease of the dissipated power and hence that of the electron density. To see this more clearly, the emission intensities are divided by the dissipated power to obtain a measure of energy efficiency of plasma species. As shown in Fig. 9c and 9d, this energy efficiency increases with increasing water content. This may be explained by that the increase of water content increases the efficiency of the Penning ionization of water molecules by helium metastables via $He^*+H_2O \rightarrow He+H_2O^+ + e$, $He^*+H_2O \rightarrow He+OH^+ + H + e$, and $He^*+H_2O_2 \rightarrow He+OH+OH^+ + e$ [72]. There appears to be an optimal window of operation for energy efficiency of plasma species production.

Similarly in the nonthermal arc mode, the optical emission intensity increases first, though more gradual than that in the bullet mode, and then undergoes a monotonic reduction in Fig. 10a. The change-over point is around F_{moist} = 40 sccm, and is consistent with the H_2O dependences of both electron density and dissipated power in Fig. 8. The exception appears to be the H line at 656 nm and helium line at 706 nm, which remain little changed. When considering energy efficiency using the dissipated power to divide into the emission intensity, the trends do not change much due to the dissipated power increasing only 24% from 6.3 to 5.1 W.

In Fig. 10c and 10d, the two N_2 lines follow similar trend as the electron density whereas the OH line intensity behaves different to all others. The latter peaks at F_{moist} = 100 sccm after which the energy efficiency of its production remains approximately constant. In Fig. 7d, T_{exc} reaches its peak at 120 sccm and T_{13} reaches its maximum at 40 sccm. When related to Fig. 10, it seems that OH(A-X) is more directly related to T_{exc} whereas all other excited species are related to T_{13} or electron density. If this is confirmed directly in future studies, it may provide methods to enable preferential reaction chemistry. The water vapour dependence of OH in Fig. 10d also suggests that the loss channel of OH through OH+OH = H_2O_2 and that of N_2 (358nm) are not as effective as other species that are seen to undergo fast decay.

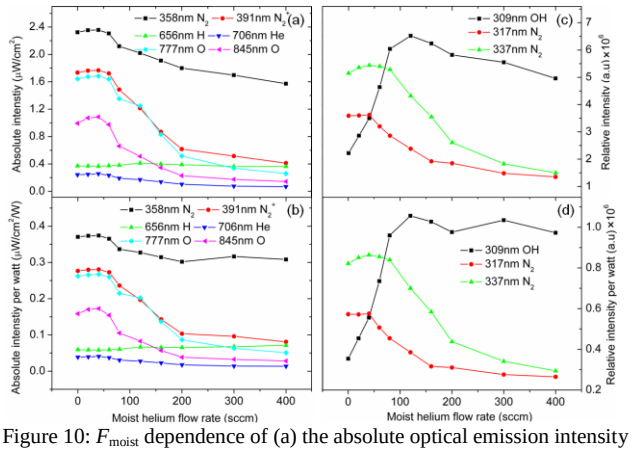

Figure 10: F_{moist} dependence of (a) the absolute optical emission intensity above 350 nm; (b) the absolute intensities per watt of dissipated power; (c) the relative optical emission intensities; and (d) the relative optical intensity per watt,, all in the nonthermal arc mode at V_{p-p} = 5.8 kV.

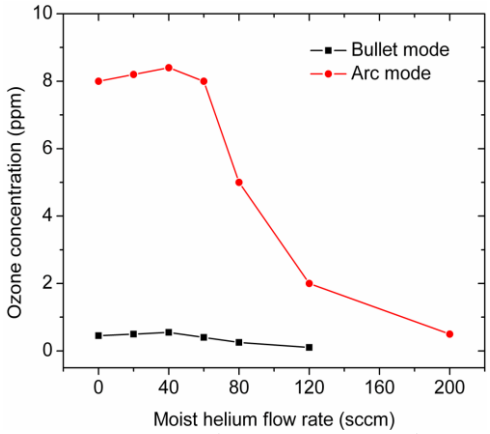

Figure 11: Moist helium flow rate dependence of ozone concentration in the bullet mode (V_{p-p} = 5kV**)** and the nonthermal arc mode (V_{p-p} = 5.8 kV).

Finally the ozone concentration is measured chemically [31] and shown as a function of the water content in Fig. 11. It is clear that the ozone production is low with its peak value at 0.7 ppm in the bullet mode and 8.4ppm in the arc mode. With increasing water content, the ozone concentration reduces significantly to below 1 ppm in both cases. The US National Institute for Occupational Safety and Health (NIOSH) recommends that the maximum ozone level is 0.1 ppm in an industrial working area (i.e. 8 hours per day and 6 days per week). The use of reasonably large quantity of water vapour would reduce the ozone concentration to 0.1ppm above 120 sccm in the bullet mode and to 0.4 ppm above 200 sccm in the arc mode. At these low levels, plasma exposure at a timescale of less than one minute per day may be become safe. Fig. 11 shows that reaction chemistry provided by the He-H_2O plasma jet is characterised by those based on OH, H_2O_2 and electrons with ozone playing a minor role having a concentration at a potentially safe level.

Figure 9 – 11 show the water content dependence of many key excited species and ozone. It is possible to adjust the water content and alter the relative proportion of different plasma species and the associated plasma chemistry. This is useful not only for manipulating plasma chemistry but also for minimising plasma species that may potentially be harmful to mammalian cells. For example water content above 120 sccm or 750ppm would reduce the ozone content to less than 0.4ppm. These data are useful in assisting the choice of the chemical composition of the plasma-forming gas for biomedical applications. An obvious related question is the specific production and loss mechanisms for each of many plasma species such as OH, H_2O_2, singlet O_2, O, and O_3. In atmospheric He-O_2 plasmas, atomic oxygen is produced mainly collisional excitation by helium metastables and their depopulation is dominated through quenching by He and O_2[31]. With water molecules involved, production and loss mechanisms are altered and in general become dependent on the water content and the dissipated electrical power [72][76]. In general, simple conclusions true for the entire parametric space are no longer always possible, due to the strong coupling of many hundreds chemical reactions, and this is an area in need of further investigation. The case of OH radicals is however becoming clearer, for which main generation and loss mechanisms are likely to be electron impact dissociation and OH+OH → H_2O_2, respectively [72][75][76].

Notwithstanding necessary *in-vitro* cell biology and *in-vivo* studies, the atmospheric He-H_2O plasma jet appears to offer an efficient and effective way to deliver desirable reaction chemistry at sub-60^oC temperature and a safe level of ozone.

6. Conclusions:

Proposed as a possible candidate for treatment of living tissues and other heat-labile material, a class of sub-60^oC atmospheric helium-water plasma jets is studied. It is shown that there are five distinct modes in the atmospheric He-H_2O plasma jet, namely the first chaotic mode, the bullet mode, the second chaotic mode, the abnormal glow mode, and the nonthermal arc mode. Mode selection and mode locking are possible by means of electrical control, thus offering a mechanism with which to operate the atmospheric He-H_2O plasma jet in a preferred mode. The observation of a chaotic mode has not been reported before in atmospheric liquid-containing plasmas, and the bullet and the second chaotic modes persist for the water vapour range 0 – 1,950ppm.

In the bullet mode, electron density, electron excitation temperature, and dissipated power simultaneously reach their maximum values all at about 40 sccm (~ 250ppm), and their water vapour dependence is mirrored in the H_2O dependence of a panel of excited plasma species (e.g. N_2, N_2^+, He, O^*, H and OH(A-X)) and ozone. In the nonthermal arc mode, the water vapour dependence of OH intensity at 309 nm and N_2 intensity at 358 nm appear to be correlated to T_{exc} whereas that of all other excited species and ozone seem to be corrected to electron density. This separate dependence may offer routes to tailor reaction chemistry of atmospheric liquid-containing plasmas. Energy efficiency of plasma species production increases with the water content, highlighting the importance of electrical power coupling, reaction chemistry, and the possibility of n_e and T_e based tailoring of downstream chemistry.

In comparison with other atmospheric liquid-containing plasmas, the He-H_2O plasma jet operated below its nonthermal arc mode has several distinct advantages, namely very low energy consumption (2 – 10 μJ per pulse), sub-60^oC gas temperature, electron-modulated production of He, N_2, N_2^+, O^*, H and OH(A-X), and low ozone production (0.1 – 0.4 ppm). In addition, it can be operated in a chaotic mode with a robust independence of the water concentration. These results provide a first attempt at the landscape of the physiochemical characteristics in atmospheric He-H_2O plasma jets.

Reference:

[1] Jones HM and Kunhardt EE 1995 *J Appl Phys* **78** 3308 – 3314.
[2] Akiyama H 2000 *IEEE Trans Dielectrics Electrical Insulation* **7** 646 – 653.
[3] Locke BR, Sato M, Sunka P, Hoffmann MR and Chang JS 2006 *Ind Eng Chem Res* **45** 882 – 905.
[4] Zhou Y, Yu SH, Cui XP, Wang CY and Chen ZY 1999 *Chem Mater* **11** 545 – 546.
[5] Xia Y, Xiong YJ, Lim B and Skrabalak SE 2009 *Angewandte Chemie Int Ed* **48** 60 – 103.
[6] Thomas HM and Morfill GE 1996 *Nature* **379** 806 – 809.
[7] Flannigan DJ and Suslick KS 2005 *Nature* **434** 52 – 55.
[8] Kong MG, Kroesen G, Morfill G, Nosenko T, Shimizu T, van Dijk J and Zimmermann JL 2009 *New J Phys* **11** 115012.
[9] Bruggeman P and Leys C 2009 *J Phys D: Appl Phys* **42** 053001.
[10] Barkun A, Bardou M, and Marshall JK 2003 *Annals Internal Medicine* **139** 843 – 885.
[11] Grund KE, Storek D and Farin G 1994 *Endosc Surg Allied Technol.* **2** 42 – 6.
[12] Sunka P 2001 *Phys. Plasmas* **8** 2587–94.
[13] Iannelli A, Bafghi AR, Patrono D, Sautot-Vial N and Gugenheim J 2006 *Obesity Surgery* **16** 1504 – 1507.
[14] Howard D and Sturtevant B 1997 *Ultrasound Med Biol* **23** 1107.
[15] Stalder K R, Mcmillen D F and Woloszko J 2005 *J Phys D: Appl Phys* **38** 1728–38.
[16] Vandamme M, Robert E, Pesnel S, Barbosa E, Dozias S, Sobilo J, Lerondel S, Le Pape A and Pouvesle JM 2010 *Plasma Process and Polymer* **7** 264 – 273.
[17] Isbary G, Morfill GE, Schmidt HU, Georgi M, Ramrath K, Heinlin J, Karrer S, Landthaler M, Shimizu T, Steffes B, Bunk W, Monetti R, Zimmermann JL, Pompl R and Stolz W 2010 *British J Dermotology*, **163** 78 – 82.
[18] Leach EH, Peters RA and Rossiter RJ 1943 *Experimental Physiology: Translation & Integration* **32** 67 – 86.
[19] De Boer JF, Srinivas SM, Malekafzali A, Chen Z and Nelson JS 1998 *Optics Express* **3** 212 – 218.
[20] Perni S, Shama G and Kong MG 2008 *J Food Protection* **71** 1619-1625.
[21] Deng XT, Shi JJ and Kong MG 2006 *IEEE Trans Plasma Sci* **34** 1310 – 1316.
[22] Lim JP, Uhm HS and Li SZ 2007 *Phys of Plasmas* **14** 093504.
[23] Perni S, Shama G, Hobman JL, Lund PA, Kershaw CJ, Hidalgo-Arroyo GA, Penn CW, Deng XT, Walsh JL and Kong MG 2007 *Appl Phys Lett* **90** 073902.
[24] Stoffels E, Sakiyama Y and Graves DB 2008 *IEEE Trans Plasma Sci* **36** 1441 – 1457.
[25] Sousa JS, Bauville G, Lacour B, Puech V, Touzeau M and Ravanat JL 2010 *Appl Phys Lett* **97** 141502.
[26] Yasuda H, Miura T, Kurita H, Takashima K, and Mizuno A 2010 *Plasma Process Polym* **7** 301 – 308.
[27] Walsh JL and Kong MG 2007 *Appl Phys Lett* **91** 251504.
[28] Shao T, Long KH, Zhang C, Yan P, Zhang SC, and Pan RZ 2008 *J Phys D: Appl Phys* **41** 215203.
[29] Iza F, Kim GJ, Lee SM, Lee JK, Walsh J, Zhang YT, and Kong MG 2008 *Plasma Process Polym* **5** 322 – 344.
[30] Kolb JF, Mohamed AAH, Price RO, Swanson RJ, Bowman A, Chiavarini RL, Stacey M and Schoenbach KH 2008 *Appl Phys Lett* **92** 241501.
[31] Walsh JL, Liu DX, Iza F, Rong MZ, and Kong MG 2010 *J Phys D: Appl Phys* **43** 032001.
[32] Walsh JL, Shi JJ and Kong MG 2006 *Appl Phys Lett* **88** 171501.
[33] Bruggeman P, Liu JJ, Degroote J, Kong MG, Vierendeels J and Leys C 2008 *J Phys D: Appl Phys* **41** 215201.
[34] Teschke M, Kedzierski J, Finantu-Dinu EG, Korzec D, and Engemann J 2005 *IEEE Trans Plasma Sci* **30** 310 – 311.
[35] Walsh JL and Kong MG 2008 *Appl Phys Lett* **93** 111501.
[36] Cao Z, Walsh JL, and Kong MG 2009 *Appl Phys Lett* **94** 021501.
[37] Cao Z, Nie QY, Bayliss DL, Walsh JL, Re CS, Wang DZ and Kong MG 2010 *Plasma Sources Sci Technol* **19** 025003.
[38] Bruggeman P, Iza F, Lauwers D and Gonzalvo YA 2010 *J Phys D: Appl Phys* **43** 012003.
[39] Chen G, Chen S, Chen W and Yang S 2008 *Surf Coating Technol* **202** 4741 – 4745.
[40] Chen Q, Kitamura T, Saito K, Haruta K, Yamano Y, Ishikawa T and Shirai H 2008 *Thin Solid Films* **516** 4435 – 4440.
[41] Zhang X, Li M, Zhou R, Feng K and Yang S 2008 *Appl Phys Lett* **93** 021502.
[42] Furusho H, Kitano K, Hamaguchi S and Nagasaki Y 2009 *Chemistry Materials* **21** 3526 – 3535.
[43] Huang D, Liang DC and Blades MW 1989 *J Anal At Spectrum* **4** 789.
[44] Anghel SD, Simon A and Frentiu T 2008 *Plasma Sources Sci Technol* **17** 045016.
[45] Albaugh J, O'Sullivan C and O'Neill L 2008 *Surf Coating Technol* **203** 844 – 847.

[46] Lee S, Peng JW and Liu CH 2009 *Carbon* **46** 2124 – 2132.
[47] Sarani A, Nikiforov AY and Leys C 2010 *Phys Plasmas* **17** 063504.
[48] Walsh JL and Kong MG 2007 *Appl Phys Lett* **91** 221502.
[49] Moon SY, Choe W, Uhm HS, Hwang YS, and Choi JJ 2002 *Phys Plasmas* **9** 4045 – 4051.
[50] Walsh JL, Iza F, Janson NB, Law VJ, and Kong MG 2009 *J Phys D: Appl Phys* **43** 075201**.**
[51] Walsh JL, Iza F, Janson NB and Kong MG, submitted and currently under review.
[52] Zhang Y, Gu BA, Peng XW, Wang DZ and Wang WC 2008 *Thin Solid Films* **516** 7547 – 7554.
[53] Deng XT and Kong MG 2004 *IEEE Trans Plasma Sci* **32** 1709 – 1715.
[54] Dawson GA and Winn WP 1965 *Z. Phys*. **183** 159.
[55] Lu X and Laroussi M 2006 *J Appl Phys* **100** 063302.
[56] Shi JJ, Zhong FC, Zhang J, Liu DW and Kong MG 2008 *Phys Plasma* **15** 013504.
[57] Bruggeman P, Schram D, Gonzalez MA, Rego R, Kong MG and Leys C 2009 *Plasma Sources Sci Technol*. **18** 025017.
[58] Laux CO, Spence TG, Kruger CH and Zare RN 2003 *Plasma Sources Sci Technol*. **12** 125 – 138.
[59] Staack D, Farouk B, Gutsol AF and Fridman AA 2006 *Plasma Sources Sci Technol* **15** 818 – 827.
[60] Kono A and Iwamoto K 2004 *Japanese J Appl Phys Pt-2* **43** L1010 – L1013.
[61] Belostotskiy SG, Khandelwal R, Wang Q, Donnelly VM, Economou DJ and Sadeghi N 2008 *Appl Phys Lett* **92** 221507.
[62] Jonkers J and Van der Mullen JAM 1999 *J Quantitative Spectro Radiative Transfer* **61** 703 – 709.
[63] Iordanova E, Palomares JM, Gamero A, Sola A and van der Mullen JJAM 2009 *J Phys D: Appl Phys* **42** 155208.
[64] Jonkers J, Vos HPC, van der Mullen JAM and Timmermans EAH 1996 *Spectrochimica Acta Pt B* **51** 457 – 465
[65] van der Mullen JAM 1990 *Spectrochimica Acta Part B - Atomic Spectroscopy* **45** 1 – 13.
[66] de Vries N, Iordanova E, Hartgers A, van Veldhuizen EM, van der Donker MJ and van der Mullen JJAM 2006 *J Phys D: Appl Phys* **36** 4194.
[67] Deng XT, Shi JJ and Kong MG 2007 J. *Appl Phys* **101** 074701.
[68] Simon A, Anghel SD, Papiu M and Dinu O 2010 *Spectrochimica Acta Part B - Atomic Spectro* **65** 272 – 278.
[69] Zhu XM and Kong MG 2005 *J Appl Phys* **97**, 083301.
[70] Porteanu HE, Kühn S and Gesche R 2010 *J Appl Phys* **108** 013301.
[71] Choi JY, Takano N, Urabe K and Tachibana K 2009 *Plasma Sources Sci Technol* **18** 035013.
[72] Liu DX, Bruggeman P, Iza F, Rong MZ and Kong MG 2010 *Plasma Sources Sci Technol* **19** 025018.
[73] Laux CO, Spence TG, Kruger CH and Zare RN 2003 *Plasma Sources Sci Technol* **12** 125 – 138.
[74] Gigosos MA and Cardenoso V 1987 *J Phys B: Atomic Mol Opt Phys* **20** 6005 – 6019.
[75] Liu DX, Rong MZ, Wang XH, Iza F, Kong MG, and Bruggeman P, 2010 *Plasma Process Polym* **7**, 846 – 865.
[76] Liu DX, Iza F, Wang XH, Kong MG, and Rong MZ, 2011, *Appl Phys Lett* **98**, 221501.